StarNet: A Deep Learning Model for Enhancing Polarimetric Radar Quantitative Precipitation Estimation

Wenyuan Li, Haonan Chen, Senior Member, IEEE, Lei Han, Member, IEEE, Wen-Chau Lee

Abstract—Accurate and real-time estimation of surface precipitation is crucial for decision-making during severe weather events and for water resource management. Polarimetric weather radar serves as the primary operational tool employed for quantitative precipitation estimation (QPE). However, the conventional parametric radar QPE algorithms overlook the dynamic spatiotemporal characteristics of precipitation. In addition, challenges such as radar beam attenuation and imbalanced distribution of precipitation data further compromise the estimation accuracy. This article develops a three-dimensional star neural network (StarNet) for polarimetric radar QPEs that integrates physical height prior knowledge and employs a reweighted loss function. To better cope with the dynamic characteristics of precipitation patterns, 3D convolution is introduced within StarNet to effectively capture the spatiotemporal features between successive radar volume scanning data. In particular, multidimensional polarimetric radar observations are utilized as inputs, and surface gauge measurements are employed as training labels. The feasibility and performance of the StarNet model are demonstrated and quantified using U.S. Weather Surveillance Radar-1988 Doppler (WSR-88D) observations collected near Melbourne, Florida. The experimental results show that the StarNet model enhances the prediction accuracy of moderate to heavy precipitation events and improves the estimation performance over long distances, with a mean absolute error (MAE) of 1.55 mm, root mean squared error (RMSE) of 2.63 mm, normalized standard error (NSE) of 25%, correlation coefficient (CC) of 0.92 and BIAS of 0.94, for hourly rainfall estimates. The results suggest that StarNet is able to effectively map the connection between polarimetric radar observations and surface rainfall.

Index Terms—quantitative precipitation estimation, dualpolarimetric radar, 3D convolutional neural network, spatiotemporal characteristics

I. INTRODUCTION

PRECIPITATION plays a crucial role in the Earth's water cycle and is an essential element in maintaining

Wenyuan Li and Lei Han were supported by the National Natural Science Foundation of China under Grant 42275003. The work of Haonan Chen was supported by the U.S. National Science Foundation (NSF) CAREER program. (Corresponding author: Lei Han.)

Wenyuan Li is with the Faculty of Information Science and Engineering, Ocean University of China, Qingdao 266100, China. She is also a visiting scholar in the Department of Electrical and Computer Engineering at Colorado State University, Fort Collins, CO 80523, USA (email: wenyuan.li@colostate.edu).

Haonan Chen is with the Department of Electrical and Computer Engineering at Colorado State University, Fort Collins, CO 80523, USA (email: haonan.chen@colostate.edu).

Lei Han is with the Faculty of Information Science and Engineering, Ocean University of China, Qingdao 266100, China.(email: hanlei@ouc.edu.cn).

Wen-Chau Lee is with the NSF National Center for Atmospheric Research (NCAR), Boulder, CO 80301, USA (email: wenchau@ucar.edu).

ecosystem balance, climate change, and human activities [1]. However, the occurrence of heavy rainfall can also serve as a catalyst for natural calamities such as floods and mudslides. With the rapid pace of urbanization, densely populated areas are becoming particularly susceptible to urban flash floods [2–5]. Hence, precise and prompt precipitation estimations play pivotal roles in flood control and water resource management.

Weather radar and rain gauges are two major measuring instruments used for observing precipitation. Weather radar can collect continuous observations over a large area with high spatial and temporal resolution (e.g., [3]). Rain gauges are ground-based observational instruments used to measure precipitation in real-time, and their observations are often used as validation data for tasks related to precipitation measurements [6, 7]. Traditional radar quantitative precipitation estimation (RQPE) methods estimate precipitation rates based on the exponential relationships between the radar reflectivity (Z) and the surface rainfall rate (R), i.e., Z-R relations. Since the inception of radar polarization [8], extensive research efforts have been dedicated to polarimetric radar systems and precipitation estimation based on polarimetric observables, encompassing radar reflectivity, differential reflectivity (Z_{dr}), and specific differential phase (K_{dp}) [9]. The radar polarimetric relationships can provide more precise microphysical information for precipitation estimation, such as the phase, size and shape of raindrops [10]. Nonetheless, the functional relationships between radar observation data and rainfall rates are typically intricate and nonlinear, as defined by explicit and generalized equations. Moreover, these power-law relations are inadequate for accurately capturing the spatiotemporal characteristics of precipitation based on radar observations. Therefore, optimizing the quantitative application of polarimetric radar by adaptively integrating the spatiotemporal characteristics of precipitation observations remains a challenge.

The past few years have witnessed the remarkable prowess of deep learning across various domains, encompassing medical image recognition, unmanned vehicles, and machine translation [11–13]. Recently, meteorological researchers have also employed neural networks in an attempt to model the relations between radar observations and rainfall rates (e.g., [14–17]) and to predict rainfall at short-term scales (i.e., precipitation nowcasting [18–23]). Simultaneously, certain researchers utilize satellite data for precipitation estimation through deep learning techniques [14, 24, 25]. In contrast to conventional approaches for precipitation estimation, deep learning employs hierarchical feature extraction and combination techniques to

1

identify patterns and correlations within the data. Our previous work demonstrated the effectiveness of applying deep learning models to the task of RQPE [15]. However, this model only focuses on the spatial characteristics of the lowest and second lowest elevation angles in radar observations while ignoring the temporal correlation between the data at each elevation angle, and the large number of parameters in this model requires a large amount of training time, which increases the computational cost and limits the flexibility of the models in practical applications. The temporal information of precipitation data is now effectively utilized in the task of precipitation forecasting [18]. However, there are limited applications in the field of precipitation estimation. In addition, the electromagnetic waves emitted by radar are subject to absorption, scattering, and refraction in the atmosphere during propagation, resulting in a gradual attenuation of signal strength with increasing distance [26]. This attenuation phenomenon adversely affects the radar's ability to accurately detect and locate precipitation, thereby reducing measurement accuracy. Particularly in cases of heavy precipitation or high atmospheric humidity, signal attenuation becomes more pronounced. Moreover, traditional parametric relations simplify precipitation formation and distribution, potentially leading to inaccuracies in portraying real precipitation patterns. For instance, they might assume a uniform distribution of precipitation over a specific area or time period, failing to capture the true variability seen in nature. Actually, precipitation events often exhibit a long-tailed distribution characterized by an abundance of weak precipitation events and a scarcity of moderate/heavy precipitation events. This phenomenon can result in the model's tendency to effectively capture the characteristics of weak precipitation during training and evaluation, while exhibiting limited capability in estimating heavy precipitation. Consequently, the model is prone to underestimating heavy precipitation as weak rainfall, leading to poor accuracy for heavy precipitation events. Overall, there are three main limitations in radar precipitation estimation, i.e., accumulated attenuation along the propagation paths, spatiotemporal feature extraction using traditional parametric radar rainfall relations, and misrepresentation of precipitation regimes of those traditional parametric relations.

To solve the above problems, the proposed approach aims to enhance the mapping capability from radar observations to precipitation. The method mainly includes three aspects of improvement:

- 1. The physical height prior information is incorporated into the radar data to convey the distance information of the sample data from the radar station. The objective of this work is to mitigate precipitation estimation errors caused by the cumulative attenuation of radar signals along the propagation paths and improve the ability of the model to capture spatiotemporal variations in precipitation over extended distances.
- 2. Aiming to enhance the model's spatiotemporal feature extraction and information transmission capabilities, this paper introduces a three-dimensional star neural network (StarNet) inspired by recurrent neural networks [27] and self-attention mechanisms [28]. The features of different layers within the network modules are interconnected and utilized iteratively to

establish a star-like information flow delivery, and the model's multi-head attention mechanism with 3D convolution further refines the spatio-temporal features of precipitation at different scales [29, 30].

3. A reweighted loss function is devised to effectively mitigate the issue of imbalanced distribution among heavy, moderate and light precipitation events. This modification enhances the model's estimation performance for moderate to heavy precipitation events, ensuring adaptability to various precipitation scenarios. Furthermore, the feasibility and performance of StarNet are demonstrated and quantified using Weather Surveillance Radar-1988 Doppler (WSR-88D) observations collected near Melbourne (KMLB), Florida, USA.

Section II introduces the study domain and datasets. Section III describes the data preprocessing and the architecture of the StarNet. Section IV presents the experimental results. A discussion and conclusion are provided in Section V.

II. STUDY DOMAIN AND DATASETS

A. Study Domain

Our study domain is situated in Florida, a region located in the southeastern United States and characterized by a tropical and subtropical climate. Due to its proximity to the equator and the influence of both the Atlantic Ocean and the Gulf of Mexico, Florida experiences high average yearround precipitation and is frequently impacted by tropical storms and hurricanes. Additionally, Florida has a flat terrain, with an average elevation of less than 30 meters, providing minimal obstruction to radar observations. Therefore, it is a region of interest for precipitation research. Fig. 1 shows the study domain for this paper, where the yellow point (80.65°W, 28.11°N) is the location of the KMLB radar site. To ensure data quality, rain gauge data within 150 km of the KMLB radar site are used in this paper. The red and black dots in Fig. 1 represent the locations of the rain gauge sites within and outside 150 km, respectively.

B. Datasets

In this article, ground radar observations are collected from KMLB Weather Surveillance Radar-1988 Doppler (WSR-88D) near Melbourne, FL. The KMLB radar is an S-band radar with a working frequency of 2.8GHz. The volume scan duration for KMLB radar ranges from 5 to 7 minutes, with a range resolution of 250 meters and an azimuth resolution of 0.5°. The KMLB radar has a maximum detection range of 460 kilometers and an elevation range from 0.5° to 19.5°. To mitigate the impact of nonprecipitation echoes on precipitation estimation in the polarimetric radar data, the DROPS2.0 data quality control algorithm is employed for their filtration and specific differential phases K_{dp} are estimated using the algorithm [31]. The rain gauge measurements utilized in this paper are sourced from the South Florida Rainfall Observation (SFL) tipping bucket rain gauge network, which is operated and managed by the South Florida Water Management District. The temporal resolution of the rain gauge data is 1 min, and the data are scalar with fixed longitudes and latitudes. The aforementioned data are also utilized as the verification

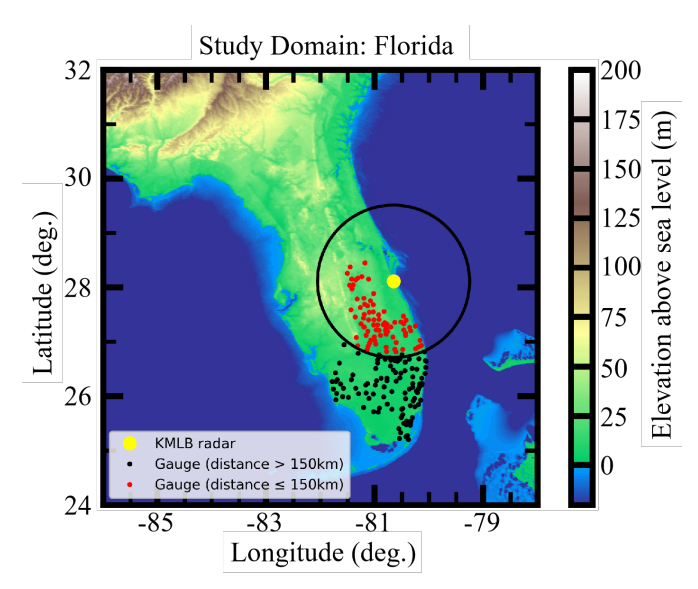


Fig. 1: Demonstration study domain in Florida, USA. The yellow dot represents the KMLB WSR-88D radar location (28.11°N, 80.65°W). The black circle indicates 150 km coverage range of the KMLB radar. The red dots and black dots indicate the distribution of rain gauges within and beyond 150 km from the radar site, respectively.

dataset for NASA's Global Precipitation Measurement (GPM) mission.

Radar and rain gauge data from 2016–2019 are utilized in this study. Specifically, the data from 2016 to 2018 are used for training (80% of the data) and validation (20% of the data), and the data from 2019 served as independent test data.

III. METHODOLOGY

Figure 2 illustrates the pipeline of our framework for QPE. It is divided into two parts: (a) the data preprocessing and (b) the deep learning framework for QPE, where Q1, Q2 and Q3 are the three questions addressed in this paper. Next, we will provide an introduction to the data preprocessing.

A. Data Preprocessing

To enhance the microphysical information of precipitation, we use three polarization radar observables radar reflectivity (Z), differential reflectivity (Z_{dr}) and specific differential phase (K_{dp}) as the model inputs, where Z_{dr} is used to describe the differences in particle shape and size within the echo, and K_{dp} characterizes the cumulative phase delay caused by water droplets of various sizes and types along the path of radar beam scanning. The rain gauge is considered the most precise equipment for monitoring precipitation as it enables direct measurement of ground-level precipitation and allows for continuous observation without time intervals. Consequently, we use rain gauge data as the ground truth for estimating precipitation.

To ensure the quality and consistency of the radar data, we applied specific thresholds and normalization procedures. Values outside this range are clipped:

- Z: The range is set between [0, 70].
- Z_{dr} : The range is set between [-1, 5].
- K_{dp} : The range is set between [-1, 10].
- Radar Observed Height: The range is set between [0, 15,000] meters.

For normalization, we employed a linear normalization method to scale these variables to a [0, 1] range using the following formula:

$$X_{norm} = \frac{X_{input} - X_{min}}{X_{max} - X_{min}} \tag{1}$$

where X_{input} is the original data, X_{norm} is the normalized data, and X_{max} and X_{min} are the maximum and minimum values, respectively.

Additionally, regions with no radar echo data are assigned a value of -1. This differentiation helps in distinguishing between areas with and without data, enhancing the model's ability to learn boundary information. These data quality measures and normalization steps are crucial for ensuring transparency and replicability of our results by other researchers.

As being introduced in Section II, KMLB dual-polarization radar observations have a temporal resolution of 5–7 minutes and a range resolution of 250 m. The temporal resolution of the rain gauge data is 1 min, and the data are scalar. Thus, there is a need to align the two data in temporal and spatial dimensions. In the temporal dimension, we take the average of the rain gauge data sums within the radar temporal resolution as the ground truth. In the spatial dimension, to align rain gauge data with radar observations accurately, we first identify the geographical coordinates (latitude and longitude) of each rain gauge. For each rain gauge site, we select the nearest radar data point as the center. Around this center point (5, 5), we extract a 9×9 pixel window from the radar data, which serves as our sample data for that particular rain gauge site.

Unlike previous related research, this paper utilizes radar data from the four lowest elevation angles and incorporates the corresponding height information for each elevation angle. The reason for this is that, as the propagation distance of the radar beam increases, there is a gradual attenuation in signal strength and an increase in vertical distance between the target detected by the radar beam and ground level, which leads to an escalation in discrepancies between the radar observations and rain gauge data, as shown in Fig. 2(a). Hence, the inclusion of height information from radar data enables deep learning models to effectively perceive both horizontal and vertical distances, thereby offering an indirect compensation for the attenuation effects. Specifically, the model is capable of more accurately estimating precipitation at various distances by analyzing radar echo data from different height layers and identifying those precipitation signals that may be underestimated due to attenuation. The scanning information of the three radar observables at different elevations is depicted in Fig. 2(a), where t, t+1, t+2 and t+3 represent the scanning times for the lowest (approximately 0.5°), 2nd lowest (approximately 0.9°), 3rd lowest (approximately 1.3°) and 4th lowest (approximately 1.8°) elevation angles, respectively. Also, t represents the time to collect radar data at different elevation angles. Similarly, H_t , H_{t+1} , H_{t+2} and H_{t+3} denote the height information for these

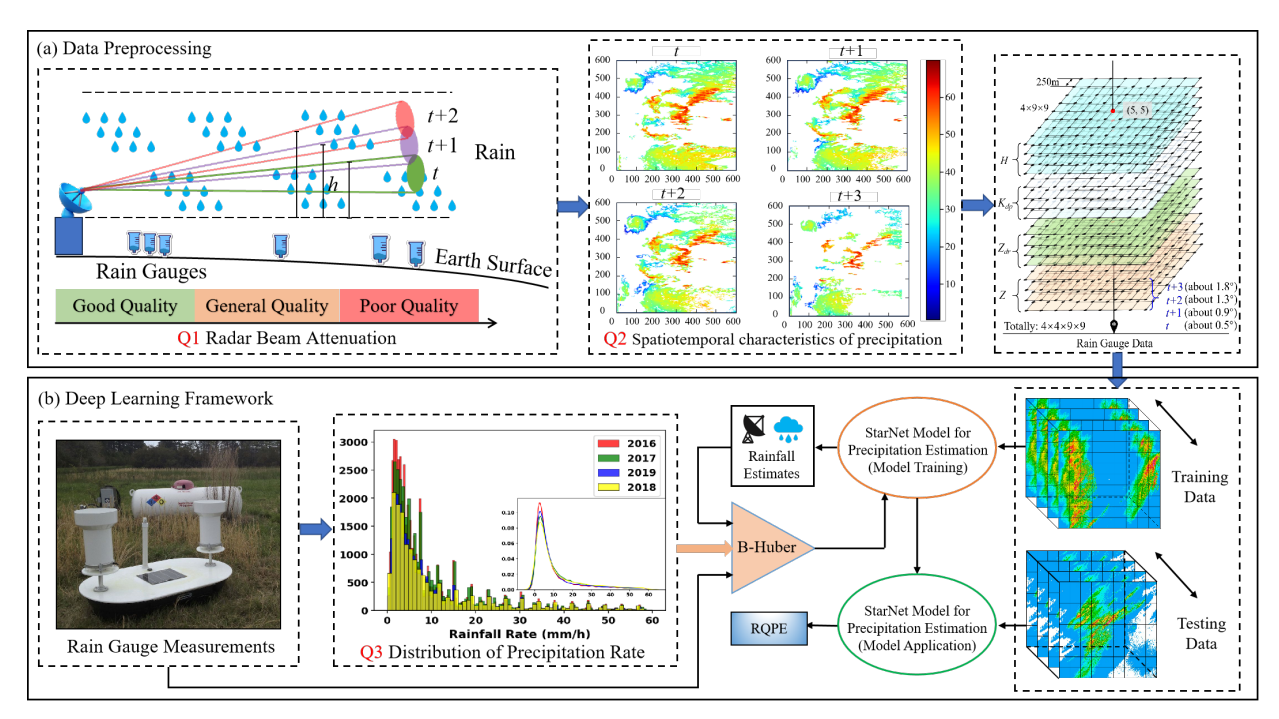


Fig. 2: Flowchart of the deep learning method for polarimetric radar QPE: (a) data preprocessing, (b) deep learning framework for QPE. Q1, Q2, and Q3 indicate issueed addressed in this article.

elevation angles. In this context, each sample is structured as a $4\times4\times9\times9$ matrix, where the first dimension represents the number of radar observables, including Z, Z_{dr} , K_{dp} , and H. The second dimension corresponds to four consecutive time points, capturing temporal dynamics. The third and fourth dimensions represent the spatial extent of the data in terms of length and width respectively.

B. Model Architecture

The proposed StarNet model architecture, depicted in Fig. 3(a), comprises four sequentially cascaded star blocks. Each block incorporates a circular connection among its layers, enhancing inter-layer feature refinement. The model's core layers incorporate 3D modules, enabling the effective processing of time-dimensional features to capture temporal variations in precipitation dynamics accurately. The estimation head module integrates features across various semantic levels during training, thereby improving precipitation estimation accuracy.

1) 3DConv Layer: Our previous research typically employs a 2D multichannel convolution method to analyze radar observations across two spatial dimensions: latitude and longitude. However, this approach often overlooks the temporal correlation inherent in precipitation patterns, specifically the variations in precipitation over time. Recent studies have demonstrated that 3D convolutional neural networks (3DCNNs) are particularly effective in various domains that involve spatiotemporal data [29]. This success is attributed to the architecture's inherent capacity to simultaneously capture both spatial and temporal information, thereby significantly enhancing the model's feature learning capabilities.

Considering precipitation as a dynamically evolving process, it becomes evident that relying solely on 2D features

is insufficient to accurately capture its complex and changing nature. The data of each radar observable at different scanning moments are superimposed in this paper, and 3D convolution is used for processing. Fig. 4 shows the 3D convolution operation of the StarNet model, whose filter size is $4\times4\times3\times3$. In contrast to 2D convolution, the 3D convolution kernel represents the height, width, and time/depth dimensions of radar data to generate a group of 3D feature maps. In this example, input features have dimensions of $4\times4\times9\times9$, corresponding to channel, time, length, and width, respectively. During convolution with a $64 \times 4 \times 4 \times 3 \times 3$ kernel, the operation extends beyond height and width, sliding across the time dimension as well, thereby effectively capturing temporal information within the feature. After the 3D convolution, the feature map is generated with the size of $64 \times 4 \times 7 \times 7$. Core components of the model, including convolution, pooling, and batch normalization, are enhanced with 3D modules for comprehensive multidimensional data processing.

2) Star Block: The cornerstone of our model is the 'star block', derived from the 3DConv layer and clique unit [30]. Its distinctive pentagram-like structure facilitates interconnected feature processing across different levels, so it is named '3DStar'. Each star block comprises two stages: stage 1 focuses on the flow of radar observation information from shallow to deep features, while stage 2 reverses this flow, facilitating the interaction and fusion of features across levels. This module allows for the transfer of information from shallow to deep convolutional units and in reverse, within the same forward propagation stage. This enhancement significantly increases the use and reuse of convolutional units and refines feature representation, aiding in the precise capture of precipitation change information. The process is illustrated in

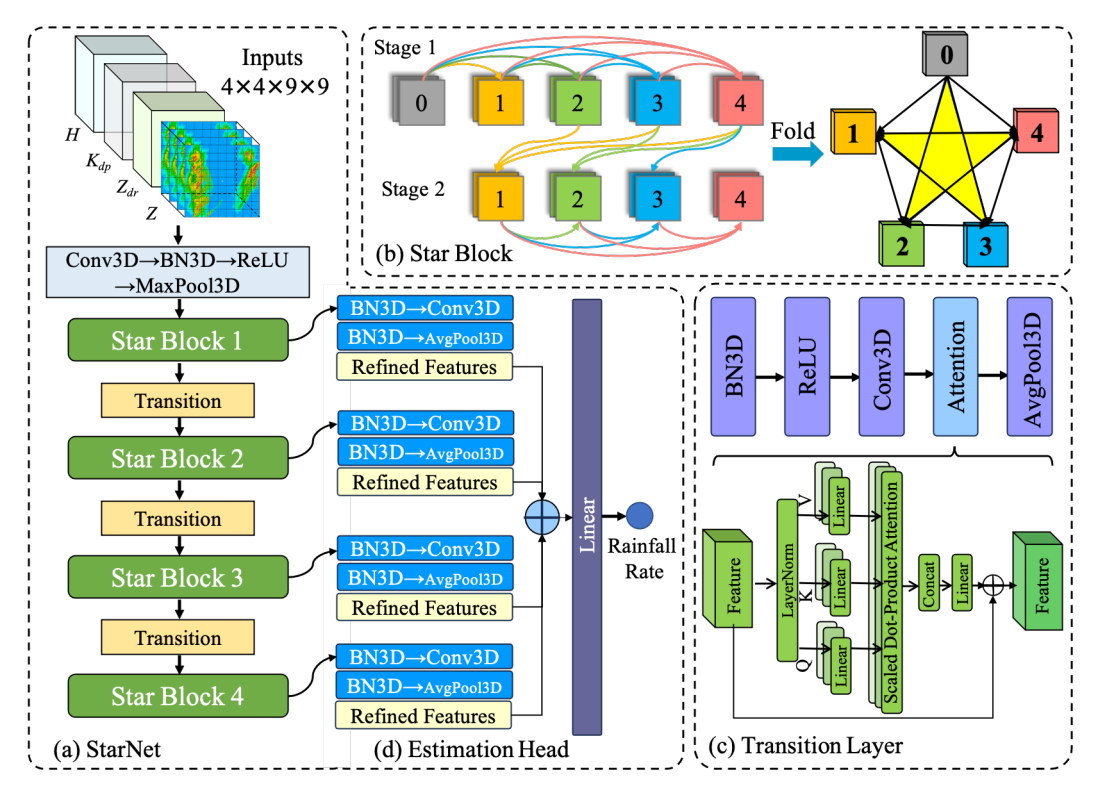


Fig. 3: The detailed architecture of StarNet: (a) StarNet, (b) Star Block, (c) Transition Layer and (d) Estimation Head. Convand BN stand for convolution and batch normalization, respectively.

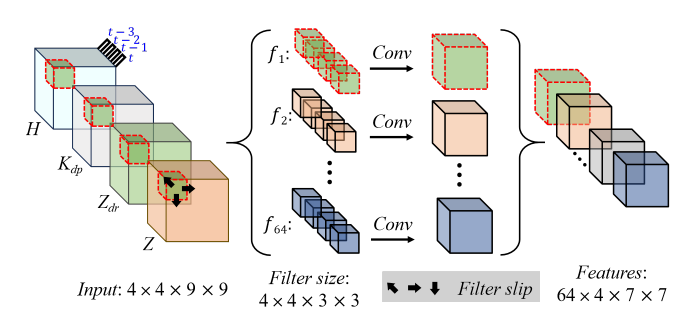


Fig. 4: The architecture of 3D convolution layer.

Fig. 3(b).

For example, in stage 1, a star block processes five depthlevel feature maps through bottleneck layers (BN3D-ReLU-3DConv(1×1) and BN3D-ReLU-3DConv(3×3)). The feature map #4, for instance, is derived as follows:

$$X_4^1 = H([X_0^1, X_1^1, X_2^1, X_3^1])$$
 (2)

where X_j^i represents the jth radar observation feature of the ith stage, with H denoting the bottleneck layer. Conversely, in stage 2, the feature input at each level comprises deeper features from stage 1 and shallower features from stage 2. For example, the input for radar observation feature #3 in stage 2 is:

$$X_3^2 = H([X_4^1, X_1^2, X_2^2])$$
 (3)

Notably, the bottleneck layers in both stages share parameters, optimizing the model's efficiency.

Our model integrates four star blocks, each consisting of six cascaded bottleneck layers, with the output channels of the 3DConv radar observation features in these blocks being 40, 80, 160 and 160, respectively.

3) Transition Layer: The transition layer in our model serves two primary functions: downsampling features and filtering critical features. This is achieved through a combination of 3D average pooling and a multi-head attention mechanism. Initially, radar observation features X_4^i from the star block undergo a 3D batch normalization layer (3DBN) and ReLU activation, followed by a 1×1 3D convolution to enhance nonlinear transformations, as shown in Fig. 3(c).

To efficiently extract precipitation information from sequence data and enhance the model's ability to differentiate between various locations and features, we have integrated a multi-head attention mechanism, as described by Vaswani et al. [32], into a residual structure. Unlike single-head attention, which focuses on a singular subset of information at any given time, multi-head attention enables the model to simultaneously attend to information from different representation subspaces at various positions. This approach with multiple 'heads' allows the model to capture a broader and more diverse range of information, significantly improving its ability to discern intricate patterns in the spatial features of precipitation data. In this process, the output from the 3DConv layer is first transformed into 2D spatial features through dimensional flattening, encompassing temporal, length, and width dimensions.

Subsequent to layer normalization, we formulate the query Q, key K, and value V vectors essential for the attention mechanism. In this setup, each element within the sequence

generates a 'query'. The mechanism then evaluates the relevance of this query in relation to a set of 'keys' linked to other elements, thus producing 'values' that signify this relevance. Such a process empowers the network to concentrate on specific segments of the input sequence that are most crucial for the task, thereby significantly enhancing its learning capabilities. Our model employs eight attention heads, with each head computing attention as per the scaled dot-product attention mechanism. The attention output of each head is computed as follows:

$$\mathbf{h}_{i} = \operatorname{Attention}(Q_{i}, K_{i}, V_{i}) = \operatorname{softmax}\left(\frac{Q_{i} K_{i}^{T}}{\sqrt{d_{k}}}\right) V_{i}, \quad (4)$$

where Q_i , K_i , and V_i are the query, key, and value matrices, respectively, for the i-th head, and d_k is the dimensionality of the keys. The function softmax is applied row-wise. Each head computes attention by first calculating the dot product of the query with the key, followed by scaling, applying the softmax function, and finally multiplying by the value. This scaled dot-product attention is a fundamental component of our transition layer, allowing it to effectively focus on different aspects of the input data in each head. The query, key, and value vectors for each head are obtained by linearly projecting the input matrix X using distinct weight matrices for each head:

$$Q_i = W_i^{(Q)} X, \quad K_i = W_i^{(K)} X, \quad V_i = W_i^{(V)} X.$$
 (5)

here, $W_i^{(Q)}$, $W_i^{(K)}$, and $W_i^{(V)}$ are the learnable parameter matrices for the query, key, and value, respectively, for the i-th attention head. The concatenated outputs of the eight attention heads are passed through a linear layer to yield enhanced features. This process can be represented by the following equation:

$$\hat{X} = X + W_o \begin{bmatrix} \mathbf{h}_1 \\ \vdots \\ \mathbf{h}_8 \end{bmatrix}$$
 (6)

In this equation, \hat{X} represents the final output of the linear layer, incorporating the residual connection. Here, $\mathbf{h}_1 \dots \mathbf{h}_8$ are the outputs of the eight attention heads, and W_o is the learnable weight matrix of the linear transformation. This structure allows the model to effectively integrate the information processed by each attention head, enhancing the feature representation derived from the input data.

Ultimately, the processed radar observation feature maps are resized back to their original four-dimensional format, after which they undergo refinement through a 3D averaging pooling layer with a stride of 2 to produce refined radar observation feature maps.

4) Estimation Head: In the estimation header module, the process begins with the aggregation of feature maps from stage 2 of each star block. These aggregated features are then compressed using a 3DBN and a 1×1 3D convolution, effectively reducing the number of channels in the feature map by half. Subsequently, a 3DBN and a 3D adaptive global pooling layer are applied, transforming these features into a

refined $1 \times 1 \times 1$ shape representation. The final step involves the concatenation of these feature streams from each block, resulting in a combined feature set. This combined feature set is then fed into a linear layer, leading to the computation of the final precipitation rate.

5) Loss Function: The estimation model for precipitation encounters significant challenges in dealing with extreme precipitation, particularly when employing the conventional mean absolute error (MAE) or mean squared error (MSE) as the loss function; the model tends to underestimate heavy rainfall rates. This is explained by the fact that the limited occurrence of heavy precipitation events in the samples hampers effective learning of such events during the model training process, resulting in a tendency to estimate strong precipitation events as weak or moderate events with larger sample sizes, as shown in Fig. 2(b). To enhance the model's ability to estimate heavy precipitation events and address dataset imbalances, this paper proposes the use of a balance-Huber (B-Huber) loss function. The initial Huber loss function is defined as follows:

$$L_{\delta}(y, e(x)) = \begin{cases} \frac{1}{2}(y - e(x))^2 & \text{for } |y - e(x)| \le \delta, \\ \delta(|y - e(x)| - \frac{1}{2}\delta) & \text{otherwise,} \end{cases}$$
(7)

where y is the actual observation, e(x) is the estimate of the model, and δ refers to the threshold hyperparameter. The model employs the MSE loss function when the error between observations and estimates is less than or equal to δ ; otherwise, it uses the MAE loss function. The Huber loss function takes advantage of the benefits of both the MAE and MSE, enabling the model to accurately fit normal values while mitigating the impact of outliers, thus improving the stability and generalizability of the model.

The B-Huber loss function proposed in this paper is based on the original Huber function and assigns varying weights to different precipitation rates. The formula is as follows:

$$L_{\text{B-Huber}}(y, e(x), r) = w(r) \times L_{\delta}(y, e(x))$$
 (8)

$$w(r) = \begin{cases} 1 & \text{if } r \le 10 \text{ mm/h,} \\ 1 + k \times (r - 10) & \text{if } 10 < r \le 40 \text{ mm/h,} \\ 1 + k \times (40 - 10) & \text{if } r > 40 \text{ mm/h,} \end{cases}$$
(9)

where r is the rainfall rate and k is the proportional factor for weight increase, which is set to 0.2 in this paper. During the experiments, setting the rainfall rate thresholds to 10 mm/h and 40 mm/h yielded optimal estimation results.

C. Comparison Methods and Evaluation Metrics

In this paper, the rainfall rate is evaluated as the cumulative amount of hourly precipitation. To demonstrate and evaluate this innovative model for mapping regional rainfall, we conducted a comparative analysis between the rainfall estimates obtained from six deep learning networks and those derived from four Z-R relations [33, 34]. These four Z-R relations are defined as follows:

$$\begin{split} R(Z) &= 1.70 \times 10^{-2} \times Z^{0.714} \quad \text{(Convective relation)} \quad \text{(4a)} \\ R(Z) &= 3.64 \times 10^{-2} \times Z^{0.625} \quad \text{(Stratiform relation)} \\ R(Z, Z_{dr}) &= 1.42 \times 10^{-2} \times Z^{0.77} \times (10^{\frac{Z_{dr}}{10}})^{-1.67} \\ \text{(NEXRAD relation)} \quad \text{(4c)} \\ R(K_{dp}) &= sign(K_{dp}) \times 54.3 |K_{dp}|^{0.806} \text{(Florida relation)} \end{split}$$

To comprehensively quantify the precipitation estimation performance of the StarNet model, eleven evaluation metrics are used in this article, which include five metrics: MAE, root mean squared error (RMSE), BIAS, correlation coefficient (CC), normalized standard error (NSE) and ubRMSE, which are computed respectively as follows:

RMSE =
$$\sqrt{\frac{\sum_{n=1}^{N} (R_n - G_n)^2}{N}}$$
 (11)

MAE =
$$\frac{\sum_{n=1}^{N} |R_n - G_n|}{N}$$
 (12)

$$CC = \frac{\sum_{n=1}^{N} (R_n - \bar{R_N})(G_n - \bar{G_N})}{\sqrt{\sum_{n=1}^{N} (R_n - \bar{R_N})^2} \sqrt{\sum_{n=1}^{N} (G_n - \bar{G_N})^2}}$$
(13)

$$NSE = \frac{\sum_{n=1}^{N} |R_n - G_n|}{\sum_{n=1}^{N} G_n}$$
 (14)

BIAS =
$$\frac{\sum_{n=1}^{N} R_n}{\sum_{n=1}^{N} G_n}$$
 (15)

ubRMSE =
$$\sqrt{\frac{\sum_{n=1}^{N} ((R_n - \bar{R_N}) - (G_N - \bar{G_N}))^2}{N}}$$
 (16)

where R_n and G_n denote the rainfall estimates and rain gauge measurements (mm) at the nth hour, respectively. N is the total number of hours, which is 3950 in our experiments. $\bar{R_N}$ and $\bar{G_N}$ represent the average of rainfall estimates and rain gauge measurements (mm) in the test dataset. When the CC and the BIAS ratios approach 1, or when the RMSE, MAE, and NSE exhibit lower values, the estimates show good performance.

In addition, five evaluation metrics are also used, namely, the probability of detection (POD), false alarm ratio (FAR), critical success index (CSI), Heidke skill score (HSS), and Gilbert skill score (GSS) are computed respectively as follows:

$$POD = \frac{S}{S + F} \tag{17}$$

$$FAR = \frac{A}{S+A} \tag{18}$$

$$CSI = \frac{S}{S + F + A} \tag{19}$$

$$HSS = \frac{2 \times (S \times N - F \times A)}{(S+F) \times (F+N) + (S+A) \times (A+N)}$$
 (20)

TABLE I: The performance of various models in precipitation estimation.

MAE (mm)	RMSE (mm)	CC	NSE (%)	BIAS (ratio)
3.26	5.07	0.76	54	0.54
3.39	5.34	0.77	56	0.48
3.34	5.15	0.78	55	0.49
2.42	3.74	0.85	40	0.81
1.77	2.99	0.89	29	0.93
1.65	2.81	0.90	27	0.92
1.64	2.78	0.91	27	0.90
1.63	2.75	0.91	27	0.91
1.60	2.74	0.91	26	0.91
1.55	2.63	0.92	25	0.94
	(mm) 3.26 3.39 3.34 2.42 1.77 1.65 1.64 1.63 1.60	(mm) (mm) 3.26 5.07 3.39 5.34 3.34 5.15 2.42 3.74 1.77 2.99 1.65 2.81 1.64 2.78 1.63 2.75 1.60 2.74	(mm) (mm) CC 3.26 5.07 0.76 3.39 5.34 0.77 3.34 5.15 0.78 2.42 3.74 0.85 1.77 2.99 0.89 1.65 2.81 0.90 1.64 2.78 0.91 1.63 2.75 0.91 1.60 2.74 0.91	(mm) (mm) CC (%) 3.26 5.07 0.76 54 3.39 5.34 0.77 56 3.34 5.15 0.78 55 2.42 3.74 0.85 40 1.77 2.99 0.89 29 1.65 2.81 0.90 27 1.64 2.78 0.91 27 1.63 2.75 0.91 27 1.60 2.74 0.91 26

$$GSS = \frac{S - Q}{S + F + A - Q} \quad Q = \frac{(S + F) \times (S + A)}{S + F + A + N} \quad (21)$$

If the radar precipitation estimates and rain gauge measurements are greater than a threshold, they are considered active, otherwise inactive. S denotes a success (i.e., both the rain gauge measurement and rainfall estimate are active); F denotes a failure (i.e., the rain gauge measurement is active, but the rainfall estimate is inactive); A denotes a false alarm (i.e., rain gauge measurement is inactive, but the rainfall estimate is active); N denotes a correct negative (i.e., rain gauge measurement and rainfall estimate are both inactive). Higher POD, CSI, HSS, GSS, or lower FAR indicate better estimation performance.

IV. EXPERIMENTS AND RESULTS

In the experimental section, we initially quantify the estimation performance of different methods using all precipitation samples. Then, we conducted a comparative analysis of the estimation performance of the nine methods at thresholds of 2.5 mm, 5.0 mm, and 7.6 mm. We also evaluate the performance of these methods in different observation ranges and loss functions. The estimation results are ultimately visualized by generating precipitation product maps.

In Table I, the precipitation estimation performance of four Z-R relations and six deep learning models are compared under all samples. It can be seen that StarNet achieves superior estimation performance, with the lowest MAE of 1.55 mm, RMSE of 2.63 mm, NSE of 25%, highest CC of 0.92 and the BIAS ratio of 0.97. The estimated results of RQPENet_{D1} are suboptimal. Fig. 5 shows a scatter plot of precipitation estimation errors for nine RQPE methods, with the horizontal axis representing cumulative hourly rain gauge measurements, the vertical axis representing the cumulative hourly precipitation estimated by the different methods. The color-coded axis uses the $y = log_{10}x$ function to indicate the sample size of each scatter, where x is the actual number of samples at a given scatter point, and y is the color-coded value in the

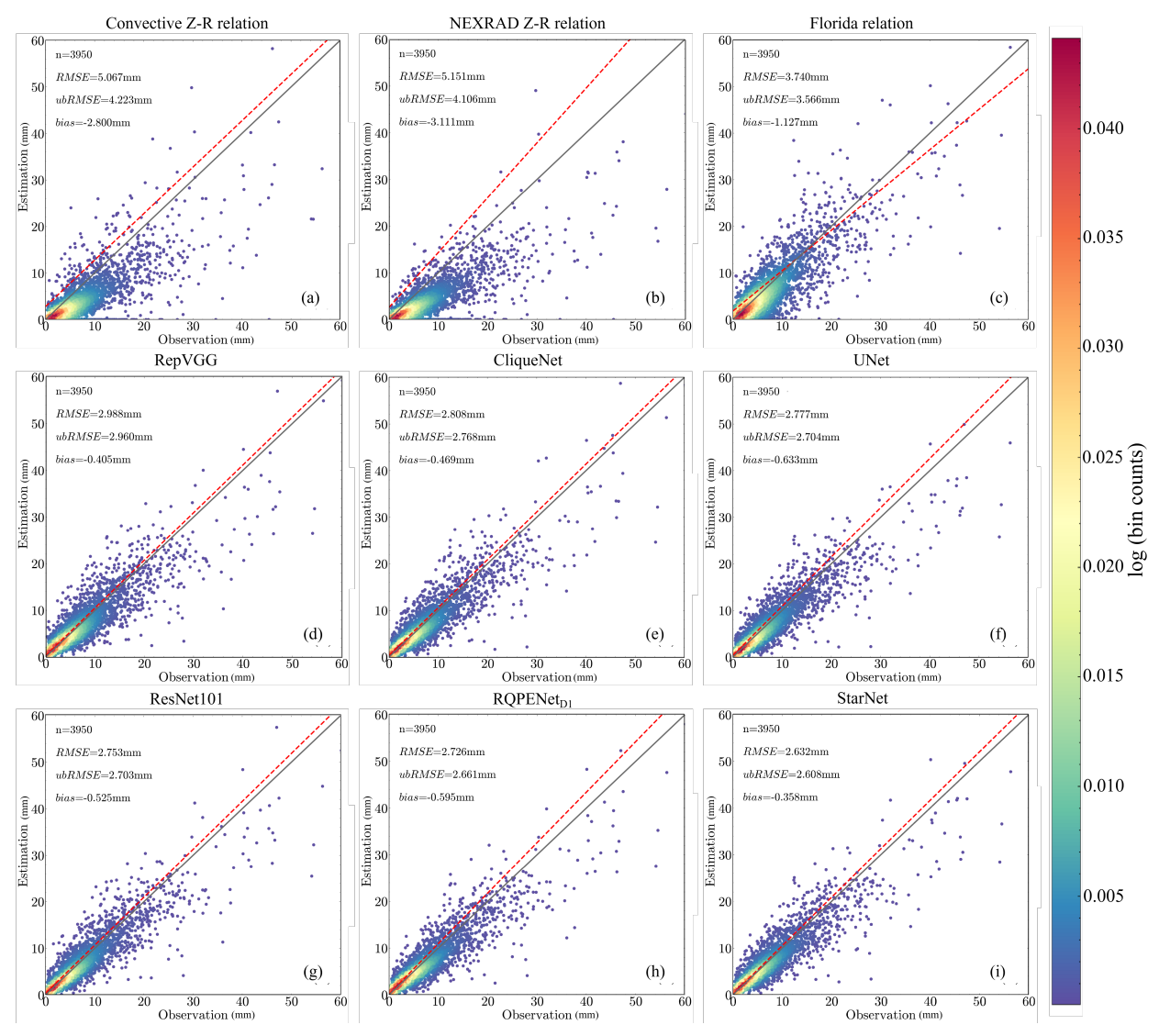


Fig. 5: Scatter plots of hourly precipitation estimates from different RQPE methods versus validation gauge observations: (a)-(c) represent convective Z-R relation, NEXRAD Z-R relation, and Florida relation, respectively, and (d)-(i) correspond to RepVGG, CliqueNet, UNet, ResNet101, RQPENet $_{\rm D1}$ and StarNet, respectively.

color range. A higher concentration of red indicates higher sample sizes while blue represents lower sample sizes. The precipitation per hour is represented by each scatter in Fig. 5. The value of n represents the cumulative number of hours, which amounts to 3950. The closer the red regression line of the scatter aligns with the diagonal, the higher the estimated accuracy. Meanwhile, we introduce two additional parameters, namely unadjusted bias root mean squared error (ubRMSE) [37] and bias, to facilitate the evaluation of different methods. The ubRMSE considers both the bias and variance in model estimation, and the bias represents the disparity between the average estimates derived from different methods and the average rain gauge measurements. As can be seen from Fig. 5(a)-(c), the scatter points of the Z-R relations have an overall downward slope, i.e., the precipitation estimates by the Z-Rrelations are lower than the rain gauge measurements. The bias value also indicates a significant disparity between the precipitation estimated by the Z-R relations and the rain gauge

measurements. Additionally, both RMSE and ubRMSE values are notably high. The scatter plots in Fig. 5(d)-(i) depict the performance of six deep learning methods in estimating precipitation. It is evident that the scatter points of the deep learning models are densely clustered around the diagonal line, indicating a closer proximity between the model's precipitation estimates and the measurements from rain gauges. This effectively mitigates the issue of underestimating precipitation. The RMSE, ubRMSE, and bias values are significantly decreased. Notably, StarNet exhibited the highest accuracy, achieving a minimal RMSE of 2.632 mm, ubRMSE of 2.608 mm, and a bias of -0.358 mm. Through the analysis of Fig. 5, it is evident that the majority of precipitation generated by precipitation events falls within the range of 0-20 mm. However, there is a scarcity of data for heavy or extreme precipitation, leading to an inadequate sample size for model training and subsequently impacting the accuracy of precipitation estimation. This deficiency is also the primary reason for the increasing discrepancy

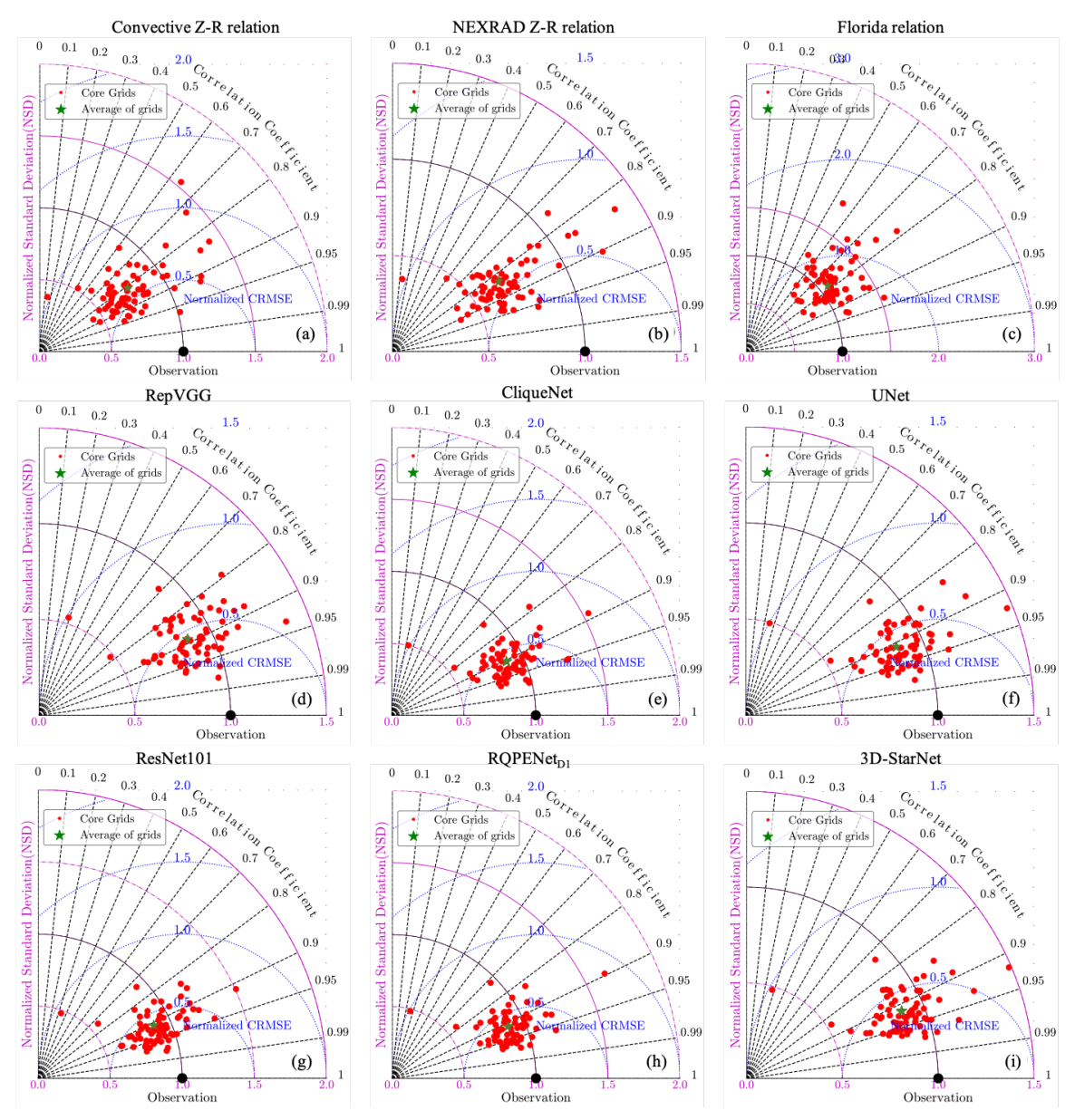


Fig. 6: Taylor plots of nine RQPE algorithms: (a)-(c) represent convective Z-R relation, NEXRAD Z-R relation, and Florida relation, respectively, and (d)-(i) correspond to RepVGG, CliqueNet, UNet, ResNet101, RQPENet_{D1} and StarNet, respectively.

between estimates and ground truths as precipitation levels rise.

To provide a more comprehensive and intuitive comparison of the performance of different RQPE methods, we employ the Taylor diagram, as illustrated in Fig. 6. When comparing multiple models, it is not straightforward to determine which model performs better or has less estimation error solely by examining the scatter plot. The Taylor diagram utilizes trigonometric geometry to visually represent three statistics - CC, normalized standard deviation (NSD), and centralized root mean square error (CRMSE) - on a single graph, facilitating a more direct comparison of model performance. In Fig. 6, the horizontal and vertical axes represent the NSD of the precipitation estimation values. The NSD helps assess the deviation between the precipitation estimates and the average

measurements of rain gauges. The radial axis denotes the correlation coefficient between estimates and measurements of rain gauges. Furthermore, the CRMSE is represented by a semicircular blue dashed line, indicating the central mean square error between the estimates and the measurements; a smaller value indicates better model estimation performance. Each red dot in the figure represents the normalized average precipitation estimate for each rain gauge. These data points are aggregated to form a green star, which represents the average estimate of the different methods and serves as an overall performance indicator for the model. Regarding overall performance, the *Z-R* relations and the RepVGG method have correlation coefficients less than 0.9 and more dispersed rain gauge points, indicating poor model performance due to low correlation between model estimates and actual values.

TABLE II: Quantitative Evaluation results of nine RQPE methods under different precipitation intensities.

Threshold		2	2.5 mm				5	.0 mm			7.6 mm						
#Sample		1	300.00	1			1	596.00			1054.00						
Total rainfall amounts (mm)		1	554.39	ı			7	568.90			14911.50						
Methods	MAE (mm)	RMSE (mm)	CC	NSE (%)	BIAS (ratio)	MAE (mm)	RMSE (mm)	CC	NSE (%)	BIAS (ratio)	MAE (mm)	RMSE (mm)	CC	NSE (%)	BIAS (ratio)		
Convective Z-R relation	0.76	1.06	0.39	64	0.55	2.79	3.31	0.33	59	0.50	7.05	8.84	0.64	50	0.56		
Stratiform Z-R relation	0.71	0.98	0.44	59	0.59	2.70	3.18	0.32	57	0.48	7.74	9.51	0.65	55	0.47		
NEXRAD relation	0.74	1.00	0.43	62	0.50	2.81	3.25	0.35	59	0.46	7.35	9.07	0.67	52	0.50		
Florida relation	1.10	1.60	0.32	92	0.79	2.12	2.72	0.43	45	0.79	4.50	6.17	0.74	32	0.83		
RepVGG [35]	0.67	1.03	0.69	56	1.46	1.38	1.91	0.52	29	0.97	3.72	5.16	0.78	26	0.86		
CliqueNet [30]	0.57	0.92	0.70	48	1.34	1.32	1.82	0.56	28	0.95	3.47	4.85	0.81	25	0.87		
UNet [36]	0.50	0.85	0.65	41	1.19	1.42	1.87	0.58	30	0.91	3.39	4.77	0.82	24	0.86		
ResNet101 [12]	0.51	0.88	0.67	43	1.26	1.37	1.83	0.58	29	0.93	3.40	4.74	0.82	24	0.87		
RQPENet _{D1} [15]	0.54	0.92	0.62	45	1.17	1.40	1.86	0.57	29	0.92	3.43	4.71	0.83	24	0.86		
StarNet	0.56	0.90	0.71	47	1.34	1.26	1.73	0.59	27	0.98	3.23	4.52	0.83	23	0.88		

TABLE III: Qualitative Evaluation results of nine RQPE methods under different precipitation intensities.

Threshold		2	2.5 mm				:	5.0 mm	ļ		7.6 mm						
Methods	POD	FAR	CSI	HSS	GSS	POD	FAR	CSI	HSS	GSS	POD	FAR	CSI	HSS	GSS		
Convective Z-R relation	0.56	0.03	0.55	0.43	0.28	0.45	0.06	0.44	0.45	0.29	0.42	0.12	0.39	0.48	0.31		
Stratiform Z-R relation	0.57	0.03	0.56	0.44	0.28	0.40	0.05	0.39	0.41	0.26	0.32	0.07	0.31	0.39	0.24		
NEXRAD relation	0.54	0.02	0.53	0.42	0.26	0.41	0.04	0.40	0.42	0.27	0.35	0.09	0.34	0.42	0.27		
Florida relation	0.76	0.08	0.72	0.58	0.41	0.70	0.12	0.64	0.64	0.47	0.67	0.17	0.59	0.66	0.49		
RepVGG [35]	0.92	0.12	0.82	0.69	0.53	0.79	0.11	0.72	0.73	0.57	0.75	0.16	0.66	0.72	0.57		
CliqueNet [30]	0.91	0.09	0.84	0.73	0.58	0.80	0.10	0.74	0.75	0.60	0.75	0.15	0.67	0.73	0.58		
UNet [36]	0.86	0.06	0.82	0.72	0.56	0.80	0.09	0.74	0.75	0.60	0.77	0.14	0.68	0.74	0.59		
ResNet101 [12]	0.89	0.07	0.83	0.73	0.58	0.81	0.09	0.75	0.76	0.61	0.76	0.15	0.67	0.74	0.58		
RQPENet _{D1} [15]	0.89	0.07	0.84	0.74	0.59	0.79	0.09	0.73	0.74	0.59	0.75	0.14	0.67	0.74	0.59		
StarNet	0.92	0.09	0.85	0.75	0.60	0.84	0.11	0.76	0.76	0.62	0.79	0.15	0.70	0.76	0.61		

Deep learning-based models such as CliqueNet, ResNet101, and RQPENet_{D1} show a general improvement in correlation coefficients to around 0.9, but still exhibit large standard deviations, indicating significant differences between model precipitation estimates and gauge measurements, thus leading to unstable performance. UNet and 3D-StarNet demonstrate the best overall performance in experiments, with correlation coefficients greater than 0.9 and closely clustered rain gauge points, showing normalized standard deviations less than 1.5, which indicates higher accuracy and reliability in their estimates. However, StarNet demonstrates better CC values and green center point values than UNet. Despite their outstanding performance, both models rely on supervised training and their effectiveness is heavily contingent upon the quantity and quality of the training data. When transitioning to regions with sparse or lower-quality data, the generalizability of these models cannot be guaranteed and necessitates further validation. Additionally, we must consider the challenges posed by different climatic conditions or geographical environments during model training.

The performance of different RQPE methods under various precipitation thresholds is presented in Table II and Table III. It can be observed from Table II that the accuracy of StarNet surpasses other methods significantly in moderate and heavy precipitation, thereby demonstrating the efficacy of the B-Huber loss function. But in weak precipitation events, UNet outperforms the StarNet model possibly due to the B-Huber loss function attenuating the performance of the latter. In Table III, except for the FAR parameter, StarNet achieves the highest POD, CSI, HSS and GSS values under 2.5 mm, 5.0 mm and 7.6 mm. For the 2mm and 5mm thresholds, the NEXRAD relation has the lowest FAR values. For the 7.6mm threshold, the Stratiform Z-R relation has the lowest FAR values. Nonetheless, it should be mentioned that CSI possesses a more comprehensive capacity for evaluating models compared to POD and FAR. In general, StarNet has the best comprehensive

TABLE IV: The performance comparison of precipitation estimation models at various distance ranges. StarNet w/o. height indicates results without using prior height information in radar data.

Threshold		:	50 km				1	00 km			150 km						
#Sample	1878							1258			814						
Methods	MAE	RMSE	CC	NSE	BIAS	MAE	RMSE	CC	NSE	BIAS	MAE	RMSE	CC	NSE	BIAS		
Methods	(mm)	(mm)	cc	(%)	(ratio)	(mm)	(mm)	cc	(%)	(ratio)	(mm)	(mm)	CC	(%)	(ratio)		
Convective Z-R relation	3.28	5.05	0.78	0.55	0.50	2.94	4.69	0.78	0.50	0.57	3.71	5.63	0.73	0.56	0.58		
Stratiform Z-R relation	3.44	5.40	0.78	0.57	0.45	3.08	5.01	0.78	0.53	0.50	3.73	5.68	0.75	0.57	0.50		
NEXRAD relation	3.39	5.18	0.80	0.56	0.46	3.07	4.89	0.79	0.52	0.51	3.65	5.47	0.76	0.55	0.52		
Florida relation	2.20	3.28	0.88	0.37	0.82	2.48	4.01	0.81	0.42	0.80	2.84	4.27	0.83	0.43	0.83		
RepVGG [35]	1.55	2.53	0.92	0.26	0.97	1.76	3.13	0.87	0.30	0.93	2.28	3.66	0.86	0.35	0.87		
CliqueNet [30]	1.45	2.42	0.93	0.24	0.93	1.67	3.00	0.88	0.28	0.91	2.07	3.30	0.88	0.31	0.94		
UNet [36]	1.47	2.41	0.93	0.25	0.90	1.67	2.98	0.89	0.29	0.90	2.00	3.21	0.89	0.30	0.89		
ResNet101 [12]	1.47	2.39	0.93	0.24	0.90	1.63	2.92	0.89	0.28	0.91	2.00	3.24	0.89	0.30	0.94		
RQPENet _{D1} [15]	1.48	2.40	0.93	0.25	0.94	1.68	2.88	0.90	0.29	0.87	2.03	3.27	0.89	0.31	0.85		
StarNet w/o. height	1.48	2.42	0.93	0.25	0.91	1.62	2.78	0.90	0.28	0.95	2.01	3.19	0.89	0.31	0.94		
StarNet	1.39	2.32	0.94	0.23	0.94	1.57	2.77	0.90	0.27	0.94	1.90	3.07	0.90	0.29	0.94		

TABLE V: Evaluation results of the StarNet under different precipitation intensities and loss functions.

Threshold	All						2.5 mm					4	5.0 mm	ì		7.6 mm					
Loss	MAE	RMSE	CC	NSE	BIAS	POD	FAR	CSI	HSS	GSS	POD	FAR	CSI	HSS	GSS	POD	FAR	CSI	HSS	GSS	
B-Huber	1.55	2.63	0.92	0.25	0.94	0.92	0.09	0.85	0.75	0.60	0.84	0.11	0.76	0.76	0.62	0.79	0.15	0.70	0.76	0.61	
MSE	1.60	2.69	0.91	0.26	0.94	0.94	0.12	0.84	0.71	0.55	0.81	0.08	0.75	0.76	0.62	0.75	0.14	0.67	0.74	0.59	
MAE	1.73	2.92	0.91	0.28	0.82	0.85	0.04	0.82	0.74	0.58	0.71	0.06	0.68	0.69	0.53	0.68	0.10	0.63	0.70	0.54	

performance.

The performance evaluation of various RQPE methods at different radar ranges is presented in Table IV. By comparing the performance of the same method across different radar area ranges, it is evident that the method's estimation performance diminishes with increasing distance and is significantly influenced by radar beam attenuation. It is worth noting that, with the exception of the StarNet w/o. height method, the other RQPE methods employed in this study all utilize radar data with height prior information. Overall, StarNet exhibits superior estimation performance compared to other methods within the radar range of 50 km, 100 km, and 150 km. Although the estimation performance of StarNet without height prior information is reduced, it still outperforms other methods. This demonstrates that incorporating height information in radar data mitigates the impact of radar beam attenuation while highlighting the superior ability of StarNet to extract spatiotemporal characteristics of precipitation.

Table V shows the comparison of the estimation performance of StarNet under different precipitation thresholds and various loss functions. It can be seen that employing the B-Huber loss function enhances the estimation accuracy across various precipitation amounts, and improves the model's performance particularly during moderate and heavy precipitation events. The reason for this is that the gradient of the loss function guides the updating of the model parameters during

training. By weighting the training weights of the medium and heavy precipitation samples, the estimation errors of these samples will produce a larger gradient, which means that when the parameters are updated, these larger error samples will have a greater impact on the learning of the model. Simultaneously, it enhances the model's capacity to learn and characterize moderate and heavy precipitation events, thereby facilitating the model to rapidly and accurately estimate heavier precipitation events. In general, the performance of the B-Huber loss function outperforms that of the MSE and MAE loss functions. Fig. 7 shows the precipitation products generated by four Z-R relations and four deep learning models at 20:00 UTC on May 13, 2019. A histogram is utilized to compare the evaluation metrics of five methods through their precipitation predictions, namely Florida relation, RepVGG, ResNet101, RQPENet_{D1} and StarNet, where "Diff." is the difference between the average of rain gauge measurements and the average of model estimates. Fig. 7 illustrates a significant underestimation of precipitation by the Z-R relations, whereas the deep learning models effectively address this issue. The evaluation metrics reveal that the estimation performance of StarNet surpasses other models significantly, with the lowest MAE of 1.23 mm, RMSE of 2.03 mm, NSE of 24%, Diff. of 0.16 mm, highest CC of 0.92 and the BIAS ratio of 1.03. In general, the StarNet precipitation estimation is closer to the ground truth value of precipitation.

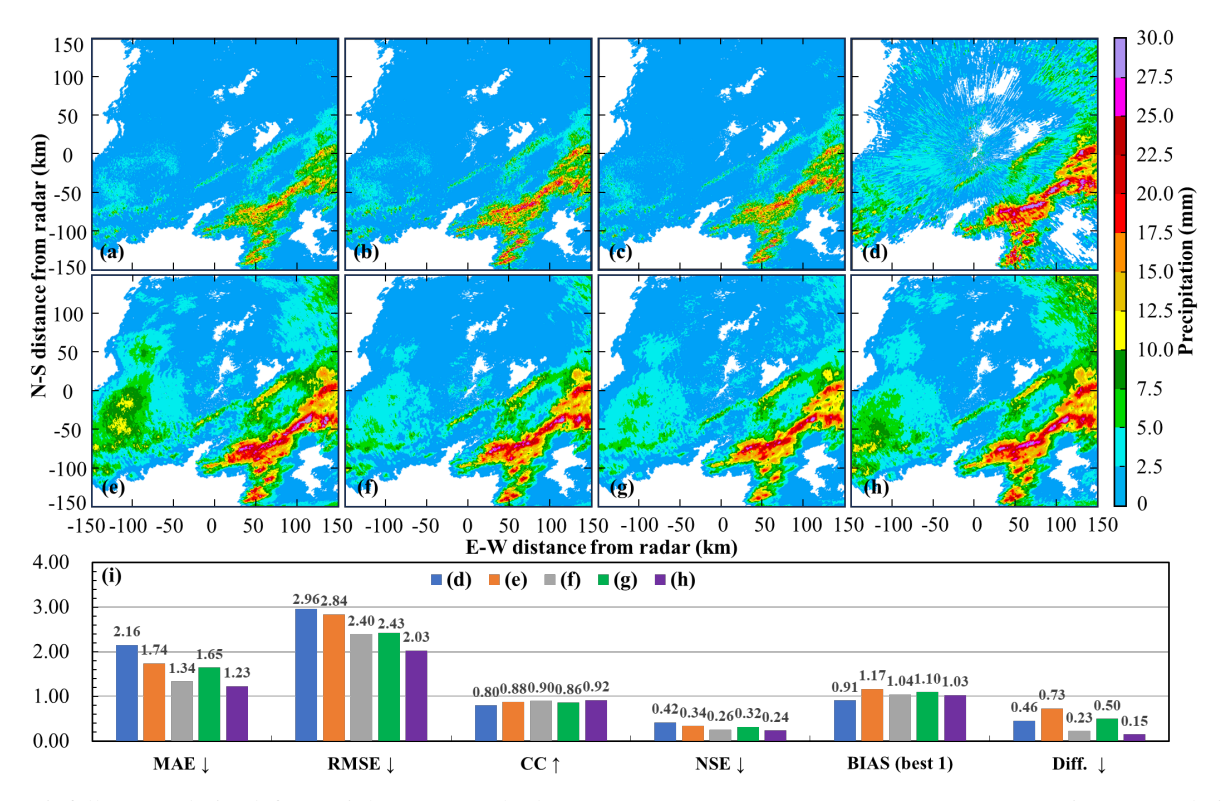


Fig. 7: Rainfall maps derived from eight QPE methods at 20:00 UTC on 13 May 2019: (a) Convective Z-R relation, (b) Stratiform Z-R relation, (c) NEXRAD relation, (d) Florida relation, (e) RepVGG, (f) ResNet101, (g) RQPENet_{D1}, (h) StarNet. Panel (i) indicates the comparison results of hourly rainfall estimates from five QPE methods.

V. SUMMARY

The current tasks of radar quantitative precipitation estimation are primarily constrained by the following limitations: accumulated attenuation along the propagation paths, spatiotemporal feature extraction using traditional parametric radar rainfall relations, and misrepresentation of precipitation regimes of those traditional parametric relations. This paper presented solutions to three problems in the current radar-based quantitative precipitation estimation:

1. Signal quality attenuation caused by radar beam propagation is mitigated by incorporating altitude information into our model. This enables the model to understand the distribution characteristics of precipitation at different heights and its impact on beam attenuation, indirectly compensating for attenuation effects. 2. The traditional parametric radar rainfall relations often lack spatiotemporal dimension feature extraction. To address this limitation, a StarNet model has been developed. This model utilizes three-dimensional convolution to extract spatiotemporal features from radar variables and significantly improves estimation performance by incorporating temporal relationships in precipitation processes. 3. Traditional parametric relations often simplify the formation and distribution of precipitation by assuming a uniform spread over a specific area or time period, but this may not accurately capture the true variability observed in nature. In fact, the distribution of precipitation events often shows a longtail pattern, where moderate and heavy precipitation events are often not well represented in the data. To improve the estimation of these events, we have developed a B-Huber loss function. This function gives more importance to these specific categories by increasing the loss weights for moderate and heavy precipitation samples.

Dual-polarization radar observations and rain gauge measurements were used in the designed deep leaning model. By utilizing ten evaluation metrics to quantify various RQPE methods across different precipitation thresholds and regions, the experimental results show that StarNet exhibits superior comprehensive performance, proving that this model can effectively extract spatiotemporal information in precipitation. Simultaneously, the incorporation of height information mitigates the impact caused by radar beam attenuation, thereby enhancing the model's performance in long-distance precipitation estimation. The experimental results of StarNet employing different loss functions show that the B-Huber loss function improves the problem of long-tailed distribution in precipitation data. Finally, the generated precipitation maps are utilized to visually demonstrate the efficacy of StarNet in polarimetric radar-based precipitation estimation.

ACKNOWLEDGMENTS

The authors gratefully acknowledge the support of NVIDIA Corporation for the donation of the GPU used for this research.

REFERENCES

[1] K. Trenberth, A. Dai, R. Rasmussen, and D. Parsons, "The changing character of precipitation," *Bulletin of*

- the American Meteorological Society, vol. 84, pp. 1205–1217, 2003.
- [2] V. Chandrasekar, H. Chen, and B. Philips, "Principles of high-resolution radar network for hazard mitigation and disaster management in an urban environment," *Journal* of the Meteorological Society of Japan. Ser. II, vol. 96, pp. 119–139, 2018.
- [3] H. Chen and V. Chandrasekar, "The quantitative precipitation estimation system for dallas–fort worth (dfw) urban remote sensing network," *Journal of Hydrology*, vol. 531, pp. 259–271, 2015.
- [4] M. Shepherd and M. Shepherd, "A review of current investigations of urban-induced rainfall and recommendations for the future," *Earth Interactions*, vol. 9, pp. 1–27, 2005.
- [5] R. Cifelli, V. Chandrasekar, L. Herdman, D. D. Turner, A. B. White, T. I. Alcott, M. Anderson, P. Barnard, S. K. Biswas, M. Boucher, J. Bytheway, H. Chen, H. Cutler, J. M. English, L. Erikson, F. Junyent, D. J. Gottas, J. Jasperse, L. E. Johnson, J. Krebs, J. van de Lindt, J. Kim, M. Leon, Y. Ma, M. Marquis, W. Moninger, G. Pratt, C. Radhakrishnan, M. Shields, J. Spaulding, B. Tehranirad, and R. Webb, "Advanced quantitative precipitation information: Improving monitoring and forecasts of precipitation, streamflow, and coastal flooding in the san francisco bay area," *Bulletin of the American Meteorological Society*, vol. 105, no. 2, pp. E313 E331, 2024.
- [6] D.-J. Seo and J. Breidenbach, "Real-time correction of spatially nonuniform bias in radar rainfall data using rain gauge measurements," *Journal of Hydrometeorology*, vol. 3, no. 2, pp. 93–111, 2002.
- [7] H. Chen, R. Cifelli, V. Chandrasekar, and Y. Ma, "A flexible bayesian approach to bias correction of radar-derived precipitation estimates over complex terrain: Model design and initial verification," *Journal of Hydrometeorology*, vol. 20, no. 12, pp. 2367 2382, 2019.
- [8] T. A. Seliga and V. Bringi, "Potential use of radar differential reflectivity measurements at orthogonal polarizations for measuring precipitation," *Journal of Applied Meteorology and Climatology*, vol. 15, no. 1, pp. 69–76, 1976.
- [9] A. Ryzhkov, P. Zhang, P. Bukovčić, J. Zhang, and S. Cocks, "Polarimetric radar quantitative precipitation estimation," *Remote Sensing*, vol. 14, no. 7, 2022.
- [10] Y. Gou, H. Chen, H. Zhu, and L. Xue, "Microphysical processes of super typhoon lekima (2019) and their impacts on polarimetric radar remote sensing of precipitation," *Atmospheric Chemistry and Physics*, vol. 23, no. 4, pp. 2439–2463, 2023.
- [11] C. Szegedy, W. Liu, Y. Jia, P. Sermanet, S. Reed, D. Anguelov, D. Erhan, V. Vanhoucke, and A. Rabinovich, "Going deeper with convolutions," in *Proceedings of the IEEE conference on computer vision and pattern recognition*, 2015, pp. 1–9.
- [12] K. He, X. Zhang, S. Ren, and J. Sun, "Deep residual learning for image recognition," in *Proceedings of the IEEE conference on computer vision and pattern recog-*

- nition, 2016, pp. 770-778.
- [13] G. Huang, Z. Liu, L. Van Der Maaten, and K. Q. Weinberger, "Densely connected convolutional networks," in Proceedings of the IEEE conference on computer vision and pattern recognition, 2017, pp. 4700–4708.
- [14] H. Chen, V. Chandrasekar, H. Tan, and R. Cifelli, "Rainfall estimation from ground radar and trmm precipitation radar using hybrid deep neural networks," *Geophysical Research Letters*, vol. 46, no. 17-18, pp. 10669–10678, 2019.
- [15] W. Li, H. Chen, and L. Han, "Polarimetric radar quantitative precipitation estimation using deep convolutional neural networks," *IEEE Transactions on Geoscience and Remote Sensing*, vol. 61, pp. 1–11, 2023.
- [16] —, "Improving explainability of deep learning for polarimetric radar rainfall estimation," *Geophysical Re*search Letters, vol. 51, no. 11, p. e2023GL107898, 2024.
- [17] Y. Zhang, S. Bi, L. Liu, H. Chen, Y. Zhang, P. Shen, F. Yang, Y. Wang, Y. Zhang, and S. Yao, "Deep learning for polarimetric radar quantitative precipitation estimation during landfalling typhoons in south china," *Remote Sensing*, vol. 13, no. 16, 2021.
- [18] X. Shi, Z. Chen, H. Wang, D.-Y. Yeung, W. Wong, and W.-c. Woo, "Convolutional lstm network: A machine learning approach for precipitation nowcasting," arXiv: Computer Vision and Pattern Recognition, arXiv: Computer Vision and Pattern Recognition, Jun 2015.
- [19] L. Han, H. Liang, H. Chen, W. Zhang, and Y. Ge, "Convective precipitation nowcasting using u-net model," *IEEE Transactions on Geoscience and Remote Sensing*, vol. 60, pp. 1–8, 2022.
- [20] S. Yao, H. Chen, E. J. Thompson, and R. Cifelli, "An improved deep learning model for high-impact weather nowcasting," *IEEE Journal of Selected Topics in Applied Earth Observations and Remote Sensing*, vol. 15, pp. 7400–7413, 2022.
- [21] L. Han, Y. Zhao, H. Chen, and V. Chandrasekar, "Advancing radar nowcasting through deep transfer learning," *IEEE Transactions on Geoscience and Remote Sensing*, vol. 60, pp. 1–9, 2022.
- [22] W. Zhang, H. Chen, L. Han, R. Zhang, and Y. Ge, "Pixel-crn: A new machine learning approach for convective storm nowcasting," *IEEE Transactions on Geoscience and Remote Sensing*, vol. 61, pp. 1–12, 2023.
- [23] A. Gong, R. Li, B. Pan, H. Chen, G. Ni, and M. Chen, "Enhancing spatial variability representation of radar nowcasting with generative adversarial networks," *Re-mote Sensing*, vol. 15, no. 13, 2023.
- [24] H. Chen, V. Chandrasekar, R. Cifelli, and P. Xie, "A machine learning system for precipitation estimation using satellite and ground radar network observations," *IEEE Transactions on Geoscience and Remote Sensing*, vol. 58, no. 2, pp. 982–994, 2020.
- [25] G. Tang, D. Long, A. Behrangi, C. Wang, and Y. Hong, "Exploring deep neural networks to retrieve rain and snow in high latitudes using multisensor and reanalysis data," *Water Resources Research*, vol. 54, no. 10, pp. 8253–8278, 2018.

- [26] S. Chumchean, A. Sharma, and A. Seed, "An integrated approach to error correction for real-time radar-rainfall estimation," *Journal of Atmospheric and Oceanic Technology*, vol. 23, no. 1, p. 67–79, Jan 2006.
- [27] L. R. Medsker, L. Jain *et al.*, "Recurrent neural networks," *Design and Applications*, vol. 5, no. 64-67, p. 2, 2001.
- [28] P. Shaw, J. Uszkoreit, and A. Vaswani, "Self-attention with relative position representations," arXiv preprint arXiv:1803.02155, 2018.
- [29] D.-K. Kim, T. Suezawa, T. Mega, H. Kikuchi, E. Yoshikawa, P. Baron, and T. Ushio, "Improving precipitation nowcasting using a three-dimensional convolutional neural network model from multi parameter phased array weather radar observations," *Atmospheric Research*, vol. 262, p. 105774, 2021.
- [30] Y. Yang, Z. Zhong, T. Shen, and Z. Lin, "Convolutional neural networks with alternately updated clique," in *Proceedings of the IEEE Conference on Computer Vision and Pattern Recognition*, 2018, pp. 2413–2422.
- [31] H. Chen, V. Chandrasekar, and R. Bechini, "An improved dual-polarization radar rainfall algorithm (drops2. 0): Application in nasa ifloods field campaign," *Journal of Hydrometeorology*, vol. 18, no. 4, pp. 917–937, 2017.
- [32] A. Vaswani, N. Shazeer, N. Parmar, J. Uszkoreit, L. Jones, A. N. Gomez, Ł. Kaiser, and I. Polosukhin, "Attention is all you need," Advances in neural information processing systems, vol. 30, 2017.
- [33] S. E. Giangrande and A. V. Ryzhkov, "Estimation of rainfall based on the results of polarimetric echo classification," *Journal of Applied Meteorology and Climatology*, vol. 47, no. 9, pp. 2445 2462, 2008.
- [34] E. A. Brandes, G. Zhang, and J. Vivekanandan, "Experiments in rainfall estimation with a polarimetric radar in a subtropical environment," *Journal of Applied Meteorology*, vol. 41, no. 6, pp. 674 685, 2002.
- [35] X. Ding, X. Zhang, N. Ma, J. Han, G. Ding, and J. Sun, "Repvgg: Making vgg-style convnets great again," in *Proceedings of the IEEE/CVF Conference on Computer Vision and Pattern Recognition*, 2021, pp. 13733–13742.
- [36] O. Ronneberger, P. Fischer, and T. Brox, "U-net: Convolutional networks for biomedical image segmentation," in *Medical Image Computing and Computer-Assisted Intervention–MICCAI 2015: 18th International Conference, Munich, Germany, October 5-9, 2015, Proceedings, Part III 18.* Springer, 2015, pp. 234–241.
- [37] D. Entekhabi, R. H. Reichle, R. D. Koster, and W. T. Crow, "Performance metrics for soil moisture retrievals and application requirements," *Journal of Hydrometeo-rology*, vol. 11, no. 3, pp. 832–840, 2010.



Wenyuan Li received the B.Sc. and M.Sc. degree in electrical engineering from Shandong University of Science and Technology, Qingdao, China, in 2017 and 2020, respectively. She is currently pursuing the Ph.D. degree in electrical engineering at the Ocean University of China, Qingdao, China. She is also a visiting scholar in the Department of Electrical and Computer Engineering at Colorado State University, Fort Collins, CO, USA. Her research interests include atmospheric remote sensing, machine learning, and explainable learning.



Haonan Chen (Senior Member, IEEE) received the Ph.D. degree in electrical engineering from Colorado State University (CSU), Fort Collins, CO, USA, in 2017

He has been an Assistant Professor in the Department of Electrical and Computer Engineering at CSU since August 2020. He is also an Affiliate Faculty with the Data Science Research Institute (DSRI) at CSU. Before joining the CSU faculty, he worked with the Cooperative Institute for Research in the Atmosphere (CIRA) and the National Oceanic

and Atmospheric Administration (NOAA) Physical Sciences Laboratory, Boulder, CO, USA, from 2012 to 2020, first as a Research Student, then a National Research Council Research Associate and a Radar, Satellite, and Precipitation Research Scientist. His research interests span a broad range of remote sensing and multidisciplinary data science, including radar and satellite remote sensing of natural disasters, polarimetric radar systems and networking, clouds and precipitation observations and processes, big data analytics, and deep learning.

Dr. Chen was a recipient of the National Science Foundation (NSF) Faculty Early Career Development Program (CAREER) Award, Ralph E. Powe Junior Faculty Enhancement Award, IEEE Geoscience and Remote Sensing Society (GRSS) Early Career Award, American Meteorological Society (AMS) Editor's Award, and CIRA Research and Service Initiative Award. He served as an Associate Editor for the Journal of Atmospheric and Oceanic Technology, URSI Radio Science Bulletin, and the IEEE JOURNAL OF SELECTED TOPICS IN APPLIED EARTH OBSERVATION AND REMOTE SENSING.



Lei Han received the B.Sc. degree in engineering mechanics and the M.Sc. degree in automatic control from Harbin Engineering University, Harbin, China, in 1998 and 2001, respectively, and the Ph.D. degree in atmospheric remote sensing from Beijing University, Beijing, China, in 2008. From 2001 to 2004, he was a Software Engineer with Lucent R&D, Qingdao, China. From 2013 to 2014, he was Visiting Scholar with the Earth Observation Laboratory (EOL), National Center for Atmospheric Research (NCAR), Boulder, CO, USA. He is cur-

rently a Professor with the College of Information Science and Engineering, Ocean University of China, Qingdao. His research interests include radar meteorology and machine learning.

PLACE PHOTO HERE Wen-Chau Lee, photograph and biography not available at the time of publication.